Real-time imaging of microparticles and living cells with CMOS nanocapacitor arrays

C. Laborde[1*], F. Pittino[2*], H. A. Verhoeven[3*], S. G. Lemay[1], L. Selmi[2], M. A. Jongsma[3] & F.P. Widdershoven[4]

Massively parallel, label free biosensing platforms can in principle be realized by combining all-electrical detection with low-cost integrated circuits. Examples include field-effect transistor (FET) arrays used for mapping neuronal signals[1,2] and DNA sequencing[3,4]. Despite these remarkable successes, however, bioelectronics has so far failed to deliver a broadly applicable biosensing platform, in no small part because DC or low-frequency signals do not allow probing beyond the electrical double layer (EDL) formed by screening salt ions[5-8]. This entails that, under physiological conditions, the sensing of target analytes located even a short distance from the sensor (~1 nm) is severely hampered. Here we demonstrate theoretically and experimentally the ability to detect and image microscale entities at long range under physiological salt conditions using high-frequency impedance spectroscopy with unprecedented spatial and temporal resolution. The assay employs a large-scale, high-density array of nanoelectrodes integrated with CMOS electronics on a single chip. The sensor response depends on the electrical properties of the analyte, allowing impedance-based fingerprinting. We also image the dynamic attachment and micromotion of BEAS, THP1 and MCF7 cancer cell lines in real time at submicron resolution in growth medium, demonstrating the potential of the platform for label/tracer-free high-throughput screening of anti-tumor drug candidates.

[1]MESA+ Institute for Nanotechnology, University of Twente, PO Box 217, 7500 AE Enschede, Netherlands. [2]DIEGM, University of Udine, Via delle Scienze 206, Udine 33100, Italy. [3]PRI-Bioscience, Wageningen University and Research Centre, PO Box 16, 6700AA Wageningen, Netherlands. [4]NXP Semiconductors, Central Research & Development / CTO office, High Tech Campus 46, 5656AE Eindhoven, Netherlands.

* These authors contributed equally to this work.

Our biosensing platform consists of a 90-nm CMOS chip (Fig. 1a) with a 256 × 256 nanoelectrode array (90 nm radius polished Au islands on a 0.6 µm × 0.89 µm grid; Fig. 1b) and integrated readout circuitry. The nanoelectrodes are row-wise selectable and column-wise individually readable. When immersed in fluid they form metal/liquid nanocapacitors. A selected row of nanocapacitors is repetitively charged/discharged at 50 MHz with a modulation voltage step V_{MOD}=245 mV via two individual MOS transistors (Fig. 1c) using all unselected nanoelectrodes in parallel as counter electrode. The charge/discharge current of a selected nanocapacitor is integrated over multiple cycles and read out via on-chip analog/digital converters. In this way we achieve high-frequency operation with attofarad resolution (standard deviation of ~1 aF at a 50 MHz modulation frequency and a frame rate of 4.8 Hz as employed here). We express the measured response signal as an equivalent switching capacitance C_{exp}, defined as the integrated charge per charge/discharge cycle divided by the modulation voltage step (See Supplementary Section I). This approach takes simultaneously advantage of three strengths of integrated circuits: high frequencies, miniaturization and large-scale integration. Although other promising concepts have been reported [9-13], this is currently the only existing biosensor platform that is capable of real time, massively parallel high-frequency impedance measurements and imaging with attofarad resolution on the submicron scale.

As first proof of concept, we sedimented 4.4 µm radius microspheres on the array surface, each sphere spanning multiple contiguous electrodes. Fig. 1d shows experimental time traces recorded from three adjacent electrodes during sedimentation. A microsphere induces position-dependent changes in the electrodes' switching capacitances, ΔC_{exp}. To quantitatively elucidate the signal transduction mechanism, we performed extensive three-dimensional finite-element simulations (Supplementary Section IV and V) based on the Poisson-Nernst-

Planck formalism[14] in the frequency domain using a numerical simulator reported previously[15]. Fig. 1e shows a map of the AC potential amplitude generated by three electrodes in 150 mM salt at zero DC bias and a 10 kHz modulation frequency typical of conventional electrochemical impedance spectroscopy[14, 16]. In this case the EDL is able to re-arrange sufficiently quickly that it essentially screens the electrode potential at all times. The instantaneous electric field thus decays exponentially from the electrode surface with a decay length equal to the equilibrium Debye screening length, λ_D (~0.8 nm at physiological salt conditions)[17]**.** Analogous to field-effect detection, the electric field in this case is only affected by the presence of a dielectric microsphere when the separation between the electrode and the sphere is of order λ_D or less (central electrode in Figure 1e). On the other hand, at modulation frequencies above a salt-concentration-dependent cutoff frequency $f_1 = 1/2\pi R_E(C_s+C_E)$, where R_E and C_E are the electrode spreading resistance and spreading capacitance, respectively, and C_s is the double-layer capacitance, the EDL no longer fully screens the applied potential (see also Supplementary Information Fig. 1). The electric field then penetrates radially into the solution, as illustrated in the potential map of Fig. 1f for 50 MHz, a frequency far above the cutoff for probing beyond the EDL $f_1 \approx 3$ MHz at 150 mM salt.

This frequency-dependent sensitivity can be directly observed experimentally. Fig. 2a shows two-dimensional maps of the measured response ΔC_{exp} of the nanoelectrode array to sedimented dielectric microspheres for three different frequencies. At 1.6 MHz (thus below the cutoff frequency f_1) the microspheres are undetectable except when they happen to land directly on an electrode (red circle), as expected from Fig. 1e. Upon increasing the frequency to 7.1 MHz and 50 MHz the microspheres have an increasingly large apparent diameter, demonstrating that EDL screening has been overcome.

To make this conclusion more quantitative, we show in Fig. 2b capacitance maps of individual beads for salt concentrations ranging from 1 mM (typical in field-effect detection experiments[18,19]) to 100 mM (near physiological conditions). Over this range λ_D changes from ~10 nm to ~1 nm. In contrast, the measured apparent radius σ_{exp} of the microparticles (σ_{exp} ~ 2.5 µm, comparable to their physical radius) is orders of magnitude larger than λ_D and independent of salt concentration. Fig. 2c shows corresponding simulated responses that are in excellent quantitative agreement with experimental results. This *ab initio* predictability is remarkable considering that most impedance spectroscopy data obtained with macroelectrodes can only be interpreted qualitatively by fitting to empirical models[16,20]. Fig. 2d further demonstrates theoretically and experimentally that microspheres of different diameters can be distinguished, illustrating that the spatial resolution is determined by solution-side processes and is not introduced by the measurement electronics. These observations represent a direct illustration that EDL screening is effectively mitigated by high-frequency operation of the nanoelectrode array.

Dielectric spheres replace high-permittivity electrolyte by a medium with much lower permittivity, repelling the electric field lines and causing C_{exp} to decrease ($\Delta C_{exp} < 0$)[21]. Conducting spheres, on the other hand, attract electric field lines, causing C_{exp} to increase ($\Delta C_{exp} > 0$). This can be used for discriminating between different particles. Fig. 3a and 3b show experimental ΔC_{exp} maps of a mixture of dielectric (latex) and conducting (gold-coated polystyrene) microspheres (both 2.5 µm radius). While the apparent particle size is similar for both cases (σ ~ 1.7 µm), the conductive microparticles show an increase in capacitance ($\Delta C_{exp} > 0$) instead of a decrease. Once again the experimental response, in particular the sign change, is well reproduced by the simulations (Fig. 3c), thus proving the ability of the physical model to capture the features of the experiment. This capability of discriminating

between particles purely based on their intrinsic electrical properties is unique to high-frequency spectroscopy, as presented here.

To explore the potential for biomedical research unlocked by combining high-frequency detection and high spatial resolution, we conducted experiments using several tumor cell lines (Fig. 4)**.** In the first experiment (Fig. 4a), K562 suspension cells were introduced on the sensor array and the cell behavior was monitored in real time. These spherical cells (diameter 15–20 μm with no prominent surface features[22]) did not exhibit attachment to the sensor surface and instead caused a response that closely resembles that of dielectric latex beads ($\Delta C_{exp} < 0$). We attribute this behavior to the presence of the insulating cellular membrane. Interestingly, an opposite sign response was obtained for dead cells (Fig. 4b). Here a droplet of BEAS cell suspension was deposited over the sensor array and dried in order to guarantee proper adhesion of the cells (Supplementary Section III). Afterwards the chip was placed in the test socket and culture medium solution with 150 mM ionic strength was introduced. Because the drying step destroys the cellular membranes of the majority of the cells, the signal is caused by the attachment of a highly concentrated layer of charged macromolecules and accompanying mobile counterions on the electrodes. This causes an increase in the measured capacitance ($\Delta C_{exp} > 0$), reminiscent of the response to conductive microparticles. In further experiments, MCF7 tumor cells were studied. Microscopic examination of these cells showed extremely high adhesion to the sensor surface with no apparent discrimination between Au electrodes and the silicon nitride regions separating them. Similarly to K562 cells, MCF7 cells generated negative signals (Fig. 4c). Intimate contact between the electrode surface and the cell membrane is supported by the observation that the much larger measured $|\Delta C_{exp}|$ compared to K562 cells corresponds to a series capacitance of 0.5 to 1.2 μF/cm^2 in series with the EDL, in good agreement with observations on nerve cells using the patch

clamp technique (0.5 to 1 $\mu F/cm^2$)[23]. Furthermore, the shape of the cells is in good agreement with SEM images[24].

Fig. 4d illustrates the attachment dynamics of MCF7 cells at one particular position on the array following their introduction into the measurement volume (markers i and ii). When the electrodes became covered by a contiguous layer of the cellular membrane (marker iii), ΔC_{exp} gradually stabilized to a value below that for uncovered electrodes. After attachment, localized fluctuations with amplitude 5–20 aF and a sub-minute time scale were detected which are attributable to the dynamics of cell adhesion and the movements of the cellular pseudopodia over the sensor surface (see also the associated video in the Supplementary Information). Fig. 4e shows time traces obtained simultaneously with Fig. 4d for five adjacent electrodes, demonstrating the gradual decrease of ΔC_{exp} during cell adhesion propagating along the array and consistent with the progressive attachment of the cells.

Since cell motility is a hallmark of the invasiveness of tumor cells, it is employed to quantify the efficacy of anti-tumor agents[25]. A cell-line specific relationship between cell motility and invasiveness involves the expression of paladin and cytoskeleton related proteins[25] which modulate the dynamics of the cell skeleton and proteolytic capacity of metastasizing tumor cells. Subcellular changes have been identified as diagnostic for the switch to invasiveness[25] and have been shown to exhibit strong relationship with sensitivity to treatment, the most invasive types being resistant to many anti-tumor agents[26,27]. The invasiveness of MCF7 cells has been shown to correlate with the presence of microvilli and pseudopodia using SEM images of fixed cells[28]. Our results on cancer cells provide a demonstration that our observations on microspheres apply as well to more complex biological systems, including the ability to detect such entities beyond the EDL, the ability to discern between entities with

different electrical transport properties, and the ability to follow detailed cell dynamics in real time. This provides a basis for developing new approaches of high-throughput screening for potential anti-tumor drugs by monitoring a range of (often difficult to assess) experimental parameters, including cell membrane area increases due to secreted vesicles, changes in motility, variations in cell shape, and membrane blebbing.

Because our sensor platform is based on a standard CMOS architecture, scalability to even better spatial and temporal resolution, larger arrays, and higher frequencies is implicitly guaranteed by the CMOS scaling roadmap. Higher frequencies are particularly interesting because above the electrolyte dielectric relaxation cutoff frequency $f_2 = 1/(2\pi R_E C_E) = \sigma_E/2\pi\varepsilon_E$ where σ_E and ε_E are the conductivity and permittivity of the electrolyte, respectively, instabilities and drift caused by adsorption of contaminants at the electrode surface are suppressed ($f_2 \approx 500$ MHz for physiological salt conditions). The sensor response then only depends on the dielectric properties of the surrounding complex medium; under these conditions, intracellular phenomena such as organelle redistribution will also become accessible.

Methods

Details of the CMOS array architecture were described previously[29]; here post-processing was also performed to cover the copper of the CMOS process with gold. Individual chips were placed in a custom-built test socket (CSP/µBGA Test & Burn socket - Aries Electronics, Inc.) mounted on a readout printed circuit board. A PDMS gasket was used to create a solution reservoir (volume ~ 50 nl) on top of the nanoelectrode array. The potential of a complete row of electrodes was switched simultaneously and the capacitive responses of the individual electrodes C_{exp} were measured. For the beads sedimentation experiment, dielectric and conducting beads were suspended in 6.6 pH PBS (0.1 mM H_3PO_4, 0.1mM KOH), and the salt concentration of the buffer solution was

further adjusted by adding KCl. The bead-containing solution was injected in the detection chamber, replacing bead-free buffer, and the sedimentation process was monitored in real time. The effective size of the particles was defined as $\sigma_{exp}^{\ 2} = \sum_i\sum_j[(i \times 0.6\ \mu m - r_{0x})^2 + (j \times 0.89\ \mu m - r_{0y})^2] \times \Delta C_{exp}(i,j) / \sum_i\sum_j \Delta C_{exp}(i,j)$ where r_{0x} and r_{0y} are the coordinates of the center of mass of the distribution and $\Delta C_{exp}(i,j)$ is the change in capacitance of electrode (i,j) after sedimentation. The same expression was used to compute σ_{th} in simulations, except that the experimental ΔC_{exp} was now replaced by its numerical approximation ΔC_{th} (Supplementary Information Section IV). For experiments with BEAS cells, a droplet with cell suspension was briefly dried over the chip before the chip was mounted in the test socket. For experiments with K562 and MCF7 cells, the flow cell was washed with PBS followed by culture medium and cells were introduced via the flow system in a flow-stopped manner operated by a manually controlled syringe. Cells were allowed to sediment to the sensor surface while the sensor response was continuously monitored.

References

1. Fromherz, P., Offenhäusser, A., Vetter, T. & Weis, J. A neuron-silicon junction: A retzius cell of the leech on an insulated-gate field-effect transistor. *Science* **252**, 1290-1293 (1991).
2. Eversmann, B. *et al.* A 128 × 128 CMOS Biosensor array for extracellular recording of neural activity. *IEEE J. Solid-State Circuits* **38**, 2306-2317 (2003).
3. Rothberg, J. M. *et al.* An integrated semiconductor device enabling non-optical genome sequencing. *Nature* **475**, 348-352 (2011).
4. Toumazou, C. *et al.* Simultaneous DNA amplification and detection using a pH-sensing semiconductor system. *Nature Methods* **10**, 641-646 (2013).
5. Matsumoto, A. & Miyahara, Y. Current and emerging challenges of field effect transistor based bio-sensing. *Nanoscale* **5**, 10702-10718 (2013).
6. Nair, P. R. & Alam, M. A. Screening-limited response of nanobiosensors. *Nano Letters* **8**, 1281-1285 (2008).
7. Rajan, N. K., Duan, X. & Reed, M. A. Performance limitations for nanowire/nanoribbon biosensors. *Wiley Interdiscip. Rev. Nanomed. Nanobiotechnol.* **5**, 629-645 (2013).
8. Stern, E. *et al.* Importance of the debye screening length on nanowire field effect transistor sensors. *Nano Letters* **7**, 3405-3409 (2007).
9. Kulkarni, G. S. & Zhong, Z. Detection beyond the Debye screening length in a high-frequency nanoelectronic biosensor. *Nano Letters* **12**, 719-723 (2012).
10. Woo, J. M. *et al.* Modulation of molecular hybridization and charge screening in a carbon nanotube network channel using the electrical pulse method. *Lab. Chip* **13**, 3755-3763 (2013).
11. Giaever, I. & Keese, C. R. A morphological biosensor for mammalian cells. *Nature* **366**, 591-592 (1993).
12. Wong, C. C. *et al.* CMOS based high density micro array platform for electrochemical detection and enumeration of cells. *Tech. Dig. Int. Electron Dev. Mtg.*, 14.2.1-14.2.4 (2013)
13. Stern, E. *et al.* Label-free immunodetection with CMOS-compatible semiconducting nanowires. *Nature* **445**, 519-522 (2007).
14. Bard, A. J. & Faulkner, L. R. *Electrochemical Methods: Fundamentals and Applications*. 2nd edn, (J. Wiley & Sons, 1980).
15. Pittino, F. & Selmi, L. Use and comparative assessment of the CVFEM method for Poisson-Boltzmann and Poisson-Nernst-Planck three dimensional simulations of impedimetric nano-biosensors operated in the DC and AC small signal regimes. *Comput. Methods in Appl. Mech. Eng.* **278**, 902-923 (2014).
16. Lasia, A. *Electrochemical Impedance Spectroscopy and its Applications*. (Springer, 2014).
17. Debye, P. & Hückel, E. Zur Theorie der Elektrolyte. I. Gefrierpunktserniedrigung und verwandte Erscheinungen. The theory of electrolytes. I. Lowering of freezing point and related phenomena. *Physik. Z.* **24**, 185-206 (1923).
18. Cui, Y., Wei, Q., Park, H. & Lieber, C. M. Nanowire nanosensors for highly sensitive and selective detection of biological and chemical species. *Science* **293**, 1289-1292 (2001).
19. Patolsky, F. *et al.* Detection, stimulation, and inhibition of neuronal signals with high-density nanowire transistor arrays. *Science* **313**, 1100-1104 (2006).

20. Daniels, J. S. & Pourmand, N. Label-free impedance biosensors: Opportunities and challenges. *Electroanalysis* **19**, 1239-1257 (2007).
21. Lorrain, P., Corson, D. P. & Lorrain, F. *Electromagnetic fields and waves.*3rd edn, (W. H. Freeman & Company, 1988).
22. Klein, E. *et al.* Properties of the K562 cell line, derived from a patient with chronic myeloid leukemia. *Int. J. Cancer* **18**, 421-431 (1976).
23. Solsona, C., Innocenti, B. & Fernández, J. M. Regulation of exocytotic fusion by cell inflation. *Biophys. J.* **74**, 1061-1073 (1998).
24. Asara, Y. *et al.* Cadmium influences the 5-Fluorouracil cytotoxic effects on breast cancer cells. *Eur. J. Histochem.* **56**, 1-6 (2012).
25. Goicoechea, S. M. *et al.* Palladin contributes to invasive motility in human breast cancer cells. *Oncogene* **28**, 587-598 (2008).
26. Verhoeven, H. A. & Van Griensven, L. J. L. D. Flow cytometric evaluation of the effects of 3-bromopyruvate (3BP) and dichloracetate (DCA) on THP-1 cells: A multiparameter analysis. *J. Bioenerg. Biomembr.* **44**, 91-99 (2012).
27. Susloparova, A., Koppenhöfer, D., Vu, X.T., Weil, M. & Ingebrandt, S. Impedance spectroscopy with field-effect transistor arrays for the analysis of anti-cancer drug action on individual cells. *Biosens. Bioelectron.* **40**, 50-56 (2010).
28. Yan, W. *et al*. Increased invasion and tumorigenicity capacity of CD44+/CD24- breast cancer MCF7 cells in vitro and in nude mice. *Cancer Cell International* **13**, 62 (2013).
29. Widdershoven, F. *et al.* CMOS biosensor platform. *Tech. Dig. Int. Electron Dev. Mtg.*, 36.1.1-36.1.4 (2010).

Acknowledgements

C.L. and S.G.L. acknowledge financial support from the European Research Council (ERC). F.P. and L.S. acknowledge financial support from the EU NANOFUNCTION project (FP7-ICT, no. 257375) and the MIUR Cooperlink project. M.A.J., H.V. and F.P.W. acknowledge financial support from NanoNextNL, a micro- and nanotechnology consortium of the Government of the Netherlands and 130 partners. F.P.W. acknowledges Eric Sterckx, Karl Verheyden, David van Steenwinckel and Ruud Hendricksen for technical support.

Author Contributions

C.L., S.G.L. and F.P.W. designed the microparticle experiments and C.L. performed them. F.P., L.S. and F.P.W. developed the numerical simulation code and F.P. executed the simulations. H.V., M.A.J. and F.P.W. designed the experiments on living cells and H.V. performed them. C.L. processed the experimental data and simulation results for the manuscript. All authors contributed to the interpretation of the results and assisted in writing the manuscript.

Additional Information

Supplementary information is available in the online version of the paper at www.nature.com/nature.

Reprints and permissions information is available online at www.nature.com/reprints. Correspondence and requests for materials should be addressed to F.P.W. (frans.widdershoven@nxp.com).

FIGURES

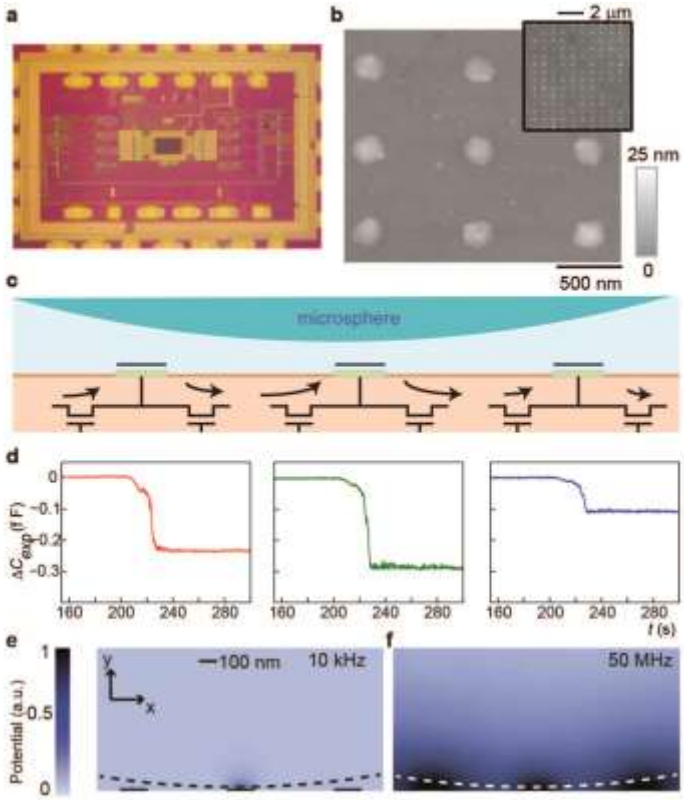

Figure 1 | **Detection principle. a,** Optical image of the CMOS chip showing the nanoelectrode array (dark rectangle) and readout circuitry (yellow and green). **b,** AFM topographic images of the nanoelectrodes. **c-d,** Each electrode is alternately charged and discharged at 50 MHz with two MOS transistors, producing a detectable average electrical measured current (black arrows). A 4.4 μm radius microsphere landing on the array perturbs the electric field generated by each electrode, inducing a position-dependent change in the current (expressed as a change in capacitance ΔC_{exp}) of three neighboring electrodes. **e,** Theoretical spatial distribution of AC potential at low frequency in 150 mM salt. The dashed line indicates the microsphere position. The electric field only penetrates a few Debye screening lengths into the solution except for the central electrode, which is positioned within a Debye length of the dielectric particle and whose field thus extends into the dielectric microsphere. **f,** AC potential amplitude at 50 MHz in 150 mM salt, where the potential extends deep into the solution.

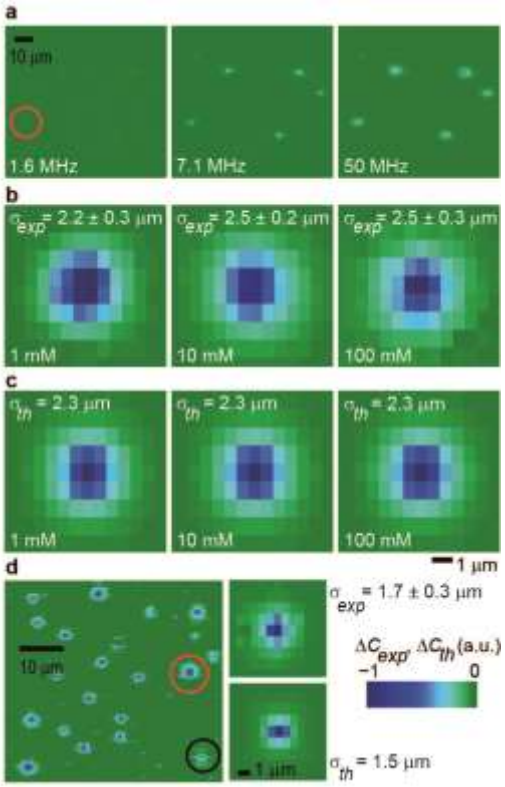

Figure 2 | Insensitivity to ionic strength. a, Spatial maps of the measured capacitance change (ΔC_{exp}) induced by the sedimentation of insulating 4.4 µm radius particles at a salt concentration of 150 mM for frequencies of 1.6 MHz, 7.1 MHz and 50 MHz. Each pixel represents a nanoelectrode and each map was normalized to the maximum value of $|\Delta C_{exp}|$. The sensitivity to the presence of microparticles increases with increasing frequency. **b,** Response to a single particle at salt concentrations of 1 mM, 10 mM and 100 mM and a frequency of 50 MHz. The rectangular shape corresponds to the asymmetry in the pitch of the array. The apparent particle size σ is independent of ionic strength over two orders of magnitude. **c,** Theoretical predictions (ΔC_{th}) for the same conditions as in **b**. **d,** Map of the array's experimental response to a mixture of two sizes of microparticles, radius 4.4 µm (red circle) and 2.5 µm (black circle) at 100 mM salt concentration. The insets show the experimental (top) and theoretical (bottom) maps for a single 2.5 µm particle.

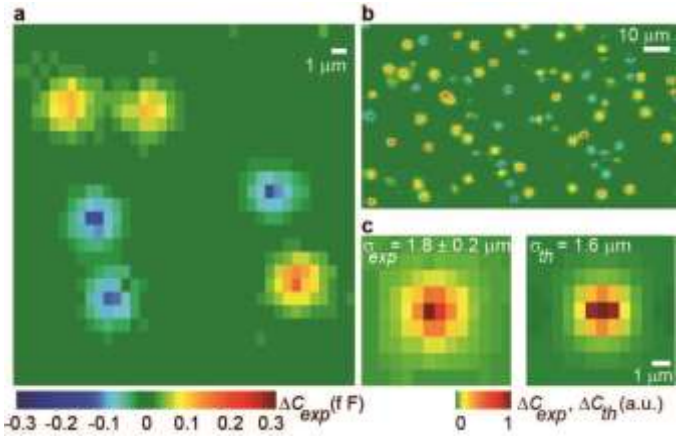

Figure 3 | **Sensitivity to particle electrical properties. a,** Response of the array to a mixture of dielectric and conducting 2.5 µm radius spheres. The signals have opposite polarities, demonstrating the ability to discriminate between two types of particles at high frequencies. **b,** Zoomed out view of figure **a**, comprising 30% of the nanoelectrode array surface. **c,** Comparison of experimental (left) and theoretical (right) capacitance maps of a conducting particle at 50 MHz and 100 mM salt.

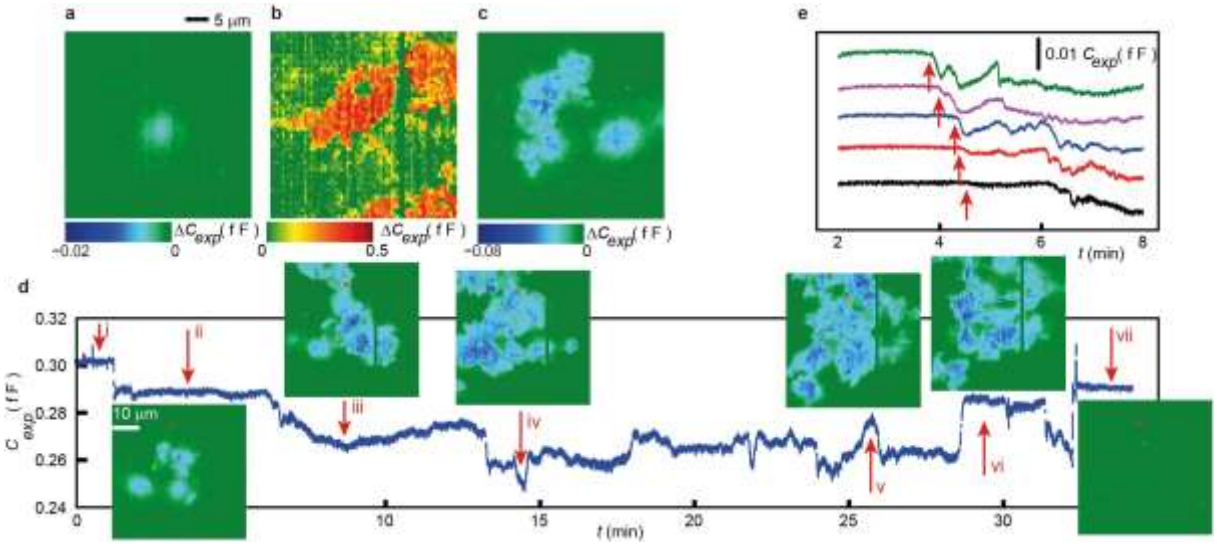

Figure 4 | **Probing living cells. a-c**, Images of three different cancer cell lines. **a,** Single K562 suspension cell in proximity of the electrodes. **b,** A clump of multiple BEAS cells attached to the electrodes. Damaged cells induce an increase in capacitance. **c,** Multiple MCF7 cells exhibiting typical strong adhesion. **d**, Single-electrode (red dot) time series during MCF7 adhesion and motion. i: PBS washing of the sensor; ii: introduction of RPMI culture medium with cells; iii: complete attachment of cells; iv– v: fluctuations due to changes in attachment of cells to the electrode surface; vi: spontaneous detachment and subsequent reattachment; vii: detachment due to washing with culture medium. **e,** The wavelike progress of cell attachment measured at 5 neighboring electrodes.